The effect of insertion layer on the perpendicular magnetic anisotropy and its electric-field-induced change at Fe/MgO interface: a first-principles investigation

IOP Publishing Journal of Physics: Condensed Matter
J. Phys.: Condens. Matter **32** (2020) 454001 (9pp) https://doi.org/10.1088/1361-648X/aba721

The effect of insertion layer on the perpendicular magnetic anisotropy and its electric-field-induced change at Fe/MgO interface: a first-principles investigation

Yurong Su[1], Jia Zhang[2,3], Jeongmin Hong[1] and Long You[1,3]

[1] School of Optical and Electronic Information, Huazhong University of Science and Technology, 430074 Wuhan, People's Republic of China
[2] School of Physics and Wuhan National High Magnetic Field Center, Huazhong University of Science and Technology, 430074 Wuhan, People's Republic of China

E-mail: jiazhang@hust.edu.cn and lyou@hust.edu.cn

Received 25 May 2020, revised 14 July 2020
Accepted for publication 17 July 2020
Published 17 August 2020

Abstract

The development of ultralow power and high density nonvolatile magnetic random access memory stimulates the search for promising materials in magnetic tunnel junction with large voltage-controlled magnetic anisotropy (VCMA) efficiency. In this work, we investigate the 4*d* and 5*d* transition metal interlayer effect on perpendicular magnetic anisotropy (PMA) and VCMA at Fe/MgO interface by using first-principles calculations. Large PMA more than 11 mJ m^{-2} is found at Fe/MgO interface with Pt insertion layer and the mechanism for PMA is clarified based on the second order perturbation theory. Furthermore, we find that the magnitude and the sign of VCMA efficiency are varied by introducing different insertions at Fe/MgO interface. The Re and Os interlayers lead to a sizable increase in both of the PMA and the VCMA coefficient. Our findings may further emphasize the essential importance of the interface structure on PMA and VCMA and may offer new material platforms for low-power consumption spintronic devices.

Keywords: voltage-controlled magnetic anisotropy, interface modification, perpendicular magnetic anisotropy, magnetic tunnel junctions, magnetization reversal

(Some figures may appear in colour only in the online journal)

1. Introduction

Spin-transfer torque offers a promising mechanism for the magnetization reversal in nonvolatile magnetic random access memory (MRAM) devices [1, 2]. However, it requires high current density and power consumption, which is about 10^7 times higher than the thermal stability limit [3]. An alternative promising approach for developing low power consumption nonvolatile MRAMs is the voltage-controlled magnetic anisotropy (VCMA) in ferromagnetic films via the voltage-controlled magnetoelectric effect [3–5]. The Fe/MgO heterostructure with perpendicular magnetic anisotropy (PMA) is one of the most promising material structures in spintronic applications [6–8]. Both theoretical investigations and experiments have evidenced that the VCMA effect can be employed in MgO-based magnetic tunnel junctions (MTJs), which has been used in the modern MRAMs and read heads [9–11]. The origin of VCMA can mainly be attributed to the spin-dependent screening of the electric field in the ferromagnetic films, and in turn the change of the 3*d* orbital occupancy of the Fe/MgO interfacial atoms with an applied electric field [9, 12, 13].

On the other hand, in order to maintain thermal stability, a large PMA is required for the nanoscale magnetic ele-

[3] Authors to whom any correspondence should be addressed.

ment, hence the VCMA should be large in order to reverse the magnetization. In the linear regime, the VCMA is proportional to the electric field inside of the insulator, i.e. VCMA $= \beta E_{\mathrm{I}}$, where β is the so-called VCMA coefficient, and E_{I} is the electric field inside of the dielectric insulator. A large VCMA effect ($\beta \sim 10^3$ fJ V^{-1} m^{-1}) is required for device application to overcome large coercivity of the ferromagnetic film. A substantial VCMA effects can be induced by voltage-controlled redox reactions, electromigration, and charge trapping with the VCMA coefficients of a few thousands of fJ V^{-1} m^{-1} [14–16]. Such large values of VCMA seem attractive but hysteretic effects are present in these cases, resulting in limited operation speed (less than the sub-millisecond range) and cycling endurance. In contrast, the VCMA caused purely by electronic effects has high speed response within sub-nanosecond regime. Unfortunately, the achieved magnitude of VCMA demonstrated at the ideal Fe/MgO(001) interface is insufficient, about 290 fJ V^{-1} m^{-1} so far [17].

Interface engineering is a promising approach to improve VCMA efficiency, since the VCMA effect originates from electronic modification at the interface of a ferromagnet and a dielectric layer. The element with large spin–orbit coupling (SOC) strength as an interface may provide a large modulation of the PMA and VCMA values. Indeed, theoretical calculations indicate that inserting heavy metal monolayers (MLs) at the interface has an impact on both the interfacial PMA and the VCMA effect [18–20]. For instance, Tsujikawa *et al* build MgO/M/Fe/Au(001) interfaces (M = Pd, Pt, and Au) and find the sign reversal of VCMA coefficient by first-principles calculations [18]. Nakamura *et al* investigate the 3*d* (Co, Ni), 4*d* (Ru, Rh, Pd), and 5*d* (Os, Ir, Pt) interlayer effect on PMA and VCMA at MgO/Fe/Au(001) interfaces by using FLAPW calculation method, and find enhanced VCMA coefficient around 300 fJ V^{-1} m^{-1} for 5*d* interlayers [19]. Experimentally, enhancement of the VCMA effect by inserting or doping ultrathin 5*d* metals Hf [21], Pt [22], W [23, 24] and Ir [25, 26] at the ferromagnetic metal/MgO interface were investigated. Especially, the Fe/MgO and FeCo/MgO interfaces with Ir doping are demonstrated to have significantly enhanced VCMA coefficients as large as 320 fJ V^{-1} m^{-1} [25] and 350 fJ V^{-1} m^{-1} [26], respectively. Other than 5*d* metals, there are also experiments showing the significant effect on the insertion of the 4*d* metal Pd in Fe(Co)/MgO systems [27–29]. It is thus interesting to systematically characterize VCMA under metal insertion at the Fe/MgO interface.

In this study, we thoroughly investigate the effect of 4*d* (Zr, Nb, Mo, Tc, Ru, Rh, Pd, Ag) and 5*d* (Hf, Ta, W, Re, Os, Ir, Pt, Au) transition metal insertions at Fe/MgO interface on the magnetic crystalline anisotropy (MCA) and the VCMA by employing the first principles calculations. Although some elements, for instance, Tc is radioactive and not applicable for practical application, we calculate the MCA for the complete 4*d* and 5*d* transition metal sets from Zr to Ag and from Hf to Au, respectively. Layer-resolved MCA study suggests that the origin of change in MCA is mainly attributed to the inserted layers. More specifically, we predict a significant enhancement of both PMA and VCMA for the ML Re and Os capped Fe(001) thin films.

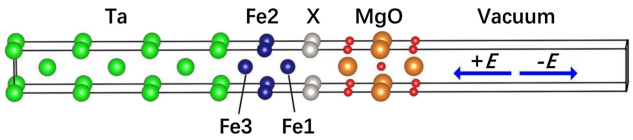

Figure 1. Schematic diagram of the computational atomic model. The blue arrows in the vacuum indicate the direction definition of the external electric field in this work.

2. Computational model and methods

For the Fe(001)/MgO interface, we use a Ta (7 ML)/Fe (3 ML)/X (1 ML)/MgO (3 ML)/vacuum (>15 Å) supercell (figure 1), in which a 4*d* (Zr, Nb, Mo, Tc, Ru, Rh, Pd, Ag) or 5*d* (Hf, Ta, W, Re, Os, Ir, Pt, Au) element X is inserted between a three-atomic Fe (in a bcc stacking) layer and a three-atomic MgO layer. As the MCA and VCMA in Fe/MgO system mainly rely on the interfacial electronic structures of Fe, it should be able to capture the main effect by using three MLs of Fe [12, 13]. Compared with the thick interlayer which may cause the decrease of TMR and deterioration of interface structure, the thin interlayer could be beneficial to the VCMA effect at Fe/MgO interface. Therefore, interlayer with thickness of one ML is chosen in the present work. The X atom sit on top of the O atom in MgO, as it is found at Fe/MgO interface [6]. Nonmagnetic seven MLs of Ta are under the Fe layers to serve as a substrate. The electric field is introduced using the dipole layer placed in the vacuum region of the supercell [30]. The definition on the direction of the applied electric field is shown in figure 1, where the positive electric field is defined as pointing away from MgO to Fe layer. The in-plane lattice constants of interlayers are constrained to the appropriate values of the bulk MgO(001) ($a = b = 2.87$ Å), while the z-positions of the whole films have been fully relaxed in the absence of electric field until the ionic Hellmann–Feynman forces on each atom are less than 1 meV Å^{-1}. After ion relaxation, the resulting atomic structures are fixed for finite electric fields in MCA calculations.

The first-principles calculations are performed by employing projector-augmented-wave (PAW) method [31], implemented in the Vienna *ab initio* simulation package (VASP) [32] within the Perdew–Burke–Ernzerhof type of generalized gradient approximation for the exchange correlation potential [33]. A plane-wave cutoff energy of 550 eV and a k-grid of $16 \times 16 \times 1$ are used to calculate the electron density self-consistently. For the calculations of MCA, a much denser k-point mesh of $32 \times 32 \times 1$ is used to converge the MCA within 10^{-5} eV per atom. The MCA is evaluated by the so-called standard force theorem. First, the electron density is calculated self-consistently in the absence of SOC. Then, one step of calculation in the presence of SOC with the magnetization pointing along different directions is performed. The MCA is evaluated by taking the energy difference between in-plane

magnetization ([100] direction) and out-of-plane magnetization ([001] direction): MCA $= E_{[100]} - E_{[001]}$. The positive MCA means the film has a PMA.

3. Results and discussions

First, we present the proximity induced magnetic moments of the inserted 4*d* and 5*d* elements in the Ta/Fe/X/MgO at zero field as shown in figure 2(a). One can find that there are large induced magnetic moments for Tc ($-0.25\ \mu_B$), Rh ($0.79\ \mu_B$), Pd ($0.33\ \mu_B$), Re ($-0.19\ \mu_B$), Os ($-0.27\ \mu_B$), Ir ($0.48\ \mu_B$) and Pt ($0.46\ \mu_B$), due to proximity hybridization between Fe and inserted atoms. When the cell size is reduced, the large PMA of the free layer is desirable to maintain the thermal stability. For instance, assuming that the diameter of the MTJ is 10 nm and its thermal stability under zero electric field is 60 k_BT, the required MCA should be larger than 3 mJ m^{-2} [4]. Figure 2(b) shows the MCA of the Fe/X/MgO structures at zero electric field. The MCA for Fe/MgO interface without insertion layer is calculated to be 1.89 mJ m^{-2}, which agrees with previous calculation results [13, 19]. We notice that early calculations find a larger MCA at FeCo/MgO interface [34, 35]. The PMA is preserved by inserting one ML of Zr, Mo, Tc, Rh, Ag, Re, Os, Pt and Au at the Fe/MgO interface, while the MCA become negative by using other 4*d* and 5*d* elemental interlayers. In particular, the presence of the interfacial Pt ML significantly enhances PMA to 11.06 mJ m^{-2} in comparison with clean Fe/MgO, while the Ir ML induces a large in-plane anisotropy of -21.83 mJ m^{-2}. The other two 5*d* interlayers Re and Os also result in enhanced PMA of 3.92 mJ m^{-2} and 3.57 mJ m^{-2}, respectively. These results indicate that it is possible to change the MCA of Fe/MgO interface significantly by inserted metal layers.

From figure 2, one can notice that, generally, for 5*d* interlayers from Re to Au with larger induced magnetic moment, the interfaces have relatively large MCA. This connection may be explained by the fact that the 5*d* interlayers have large SOC constants, and in consequence, they will play a more important contribution to MCA. However, the MCA is not fully related with the induced magnetic moment, because the former is mainly contributed by the electronic structures around the Fermi energy, while the latter originates from the whole density of states (DOS) below the Fermi energy.

It would be interesting to clarify the possible mechanism of enhanced PMA in Ta/Fe/X/MgO. Especially, here we try to discuss the origin of giant PMA with Pt interlayer. To get insight into the inserted layer effect on the MCA, first the layer-resolved MCA is evaluated by taking the SOC energy (E_{soc}) difference on each atom when the magnetization is along x (M_x) and z (M_z) directions as follows [36]:

$$\mathrm{MCA}^i \approx \frac{1}{2}(E^i_{\mathrm{soc}}(M_x) - E^i_{\mathrm{soc}}(M_z)), \tag{1}$$

where i is the atom index and a positive MCA^i indicate that the atomic layer favors PMA. We discuss in detail on how the SOC has been included in VASP–PAW theory framework and the decomposition of SOC energy onto each atom in appendix B. Figure 3(a) presents the on-site projected MCA of the Ta

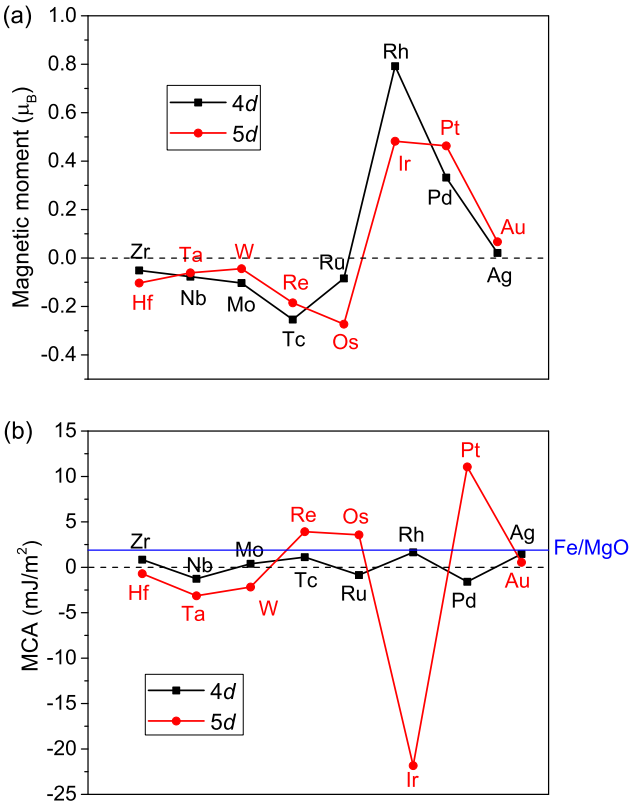

Figure 2. (a) The induced magnetic moments on the inserted transition metal atoms and (b) the MCA for Ta/Fe/X/MgO at zero electric field, where X is 4*d* (Zr, Nb, Mo, Tc, Ru, Rh, Pd, Ag) or 5*d* (Hf, Ta, W, Re, Os, Ir, Pt, Au) transition metal.

(7 ML)/Fe (3 ML)/Pt (1 ML)/MgO (3 ML). The Pt layer contributes the most of the positive MCA which is as large as 6.08 meV per unit cell. This may be related to the sizable induced magnetic moment and the large SOC constant of Pt.

The SOC Hamiltonian can be written as:

$$H_{\mathrm{soc}} = \xi\vec{\sigma}\cdot\vec{L}, \tag{2}$$

where $\vec{L}$ is the orbital angular momentum operator, $\vec{\sigma}$ is the Pauli matrix, ξ is the atomic SOC constant which is the integrated radial SOC strength $\xi = \langle\xi(r)\rangle = \left\langle \frac{\hbar^2}{4m^2c^2r}\frac{\mathrm{d}V(r)}{\mathrm{d}r}\right\rangle$. For the Fe 3*d* orbital, the integrated value ξ is around 30 meV. The SOC Hamiltonian H_{soc} is a 2×2 operator matrix and can be written as:

$$H_{\mathrm{soc}} = \begin{pmatrix} H^{\uparrow\uparrow}_{\mathrm{soc}} & H^{\uparrow\downarrow}_{\mathrm{soc}} \\ H^{\downarrow\uparrow}_{\mathrm{soc}} & H^{\downarrow\downarrow}_{\mathrm{soc}} \end{pmatrix}. \tag{3}$$

Based on the second order perturbation theory, the energy correction due to SOC can be expressed as the summation of spin-conserved terms ($E^{\uparrow\uparrow}$, $E^{\downarrow\downarrow}$) and spin-flipped terms ($E^{\uparrow\downarrow}$, $E^{\downarrow\uparrow}$) [37, 38]:

$$\Delta E = E^{\uparrow\uparrow} + E^{\downarrow\downarrow} + E^{\uparrow\downarrow} + E^{\downarrow\uparrow}, \tag{4}$$

$$E^{\alpha,\beta} = \xi^2 \sum_{\varepsilon^\alpha_o,\varepsilon^\beta_u} \frac{\left|\left\langle\psi^\alpha_o\right| H^{\alpha\beta}_{\mathrm{soc}} \left|\psi^\beta_u\right\rangle\right|^2}{\varepsilon^\alpha_o - \varepsilon^\beta_u}; \quad (\alpha,\beta = \uparrow,\downarrow), \tag{5}$$

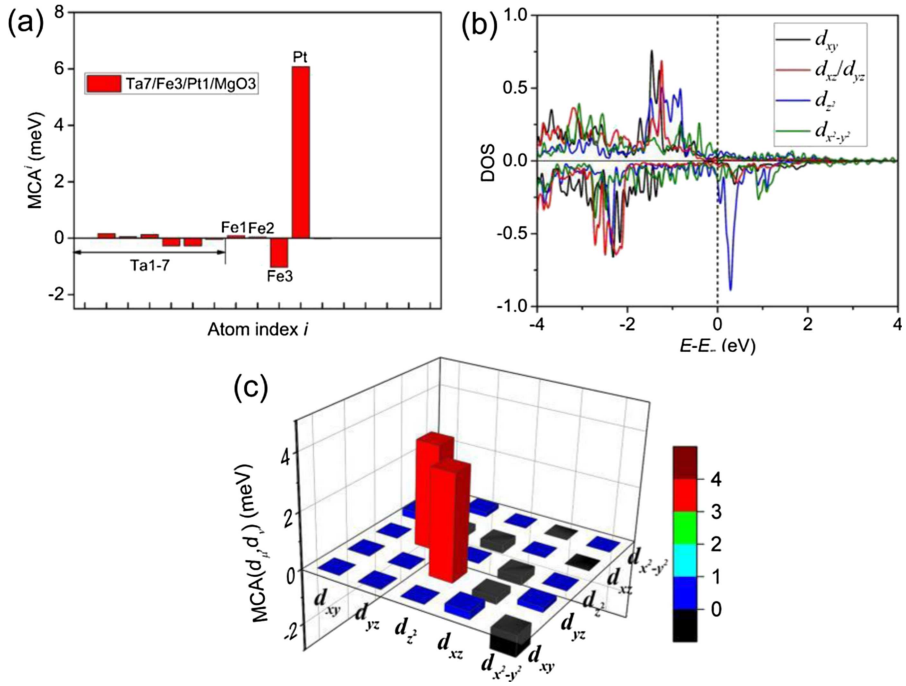

Figure 3. (a) The layer-resolved MCA, (b) the DOS in Pt in Ta/Fe/Pt/MgO structure, and (c) the d-orbital resolved MCA in Pt atomic layer.

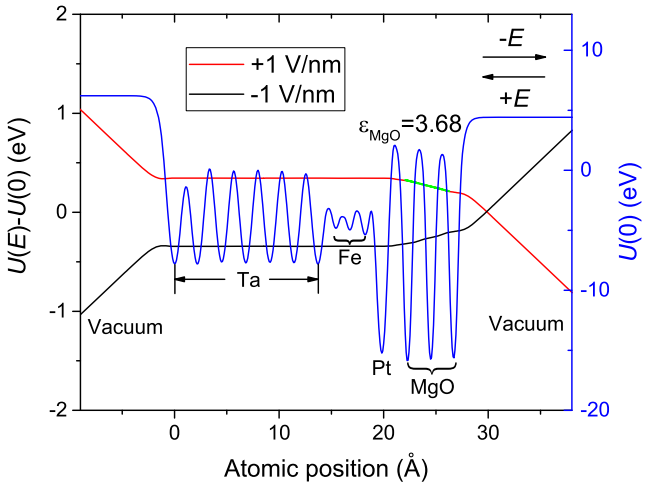

Figure 4. The planar-averaged electrostatic potential energy ($U(0)$) distribution across the Ta/Fe/Pt/MgO supercell structure at zero electric field (blue line refers to the right axis) and the change of the electrostatic potential energy ($U(E) - U(0)$) when the electric fields $E_{\rm vac} = +1$ V nm^{-1} (red line refers to the left axis) and $E_{\rm vac} = -1$ V nm^{-1} (black line refers to the left axis) are applied across the film. The arrows indicate the direction of the electric field. The green line indicates the slope of potential drop in MgO.

where ψ_o^α and ψ_u^β are unperturbed wave functions for occupied states (below Fermi energy) and unoccupied states (above Fermi energy) with energies $\varepsilon_o^\alpha$and ε_u^β, respectively. For collinear magnetic system, $(\vec{\sigma}\cdot\vec{L})$ operator and thus $H_{\rm soc}$ depend on the magnetization direction $M(\theta, \phi)$, where (θ, ϕ) are the Euler angles of magnetization $\boldsymbol{M}$. Therefore the corresponding energy correction is magnetization direction dependent. Further, by integrating over the $\boldsymbol{k}$ space, the energy correction in equation (5) can be approximately expressed by the production of DOS and the matrix elements of $H_{\rm soc}$ operator between different pair of d orbitals:

$$\Delta E = \xi^2 \sum_{\mu,\mu'} P_{\mu\mu'}^{\alpha\beta} \int_{-\infty}^{\varepsilon_{\rm F}} {\rm d}\varepsilon \int_{\varepsilon_{\rm F}}^{\infty} {\rm d}\varepsilon' \frac{\rho_\mu^\alpha(\varepsilon)\rho_{\mu'}^\beta(\varepsilon')}{\varepsilon - \varepsilon'},$$

$$P_{\mu\mu'}^{\alpha\beta} = \left| \langle d_\mu | \, (\vec{\sigma}\cdot\vec{L})_{M(\theta,\phi)}^{\alpha,\beta} \, | d_{\mu'} \rangle \right|^2, \qquad (6)$$

where d_μ is one of the five d-orbitals (d_{xy}, d_{yz}, d_{xz}, d_{z^2}, $d_{x^2-y^2}$) denoted by the orbital index μ. $\rho_\mu^\alpha(\varepsilon)$ is the DOS of d_μ orbital with spin index α. $\varepsilon_{\rm F}$ is the Fermi energy. Based on equations (5) and (6), one can find that the SOC energy correction is always negative, and therefore when magnetization is along a particular direction $M(\theta, \phi)$, the non-vanishing matrix element of $H_{\rm soc}^{\alpha\beta}$ will contribute to the energy correction and favor the magnetization along this direction (please see the appendix A for the detailed discussion on the $H_{\rm soc}^{\alpha\beta}$ matrix elements). In addition, the MCA is closely related to the distribution of DOS around the Fermi energy.

The d-orbital resolved DOS of Pt in Ta/Fe/Pt/MgO is shown in figure 3(b), which is spin-dependent and lead to relative large magnetic moment (0.46 $\mu_{\rm B}$) on Pt. The DOS of majority spin is almost fulfilled (occupied) and there are (d_{xy}, d_{yz}, d_{xz}) DOS peaks located closely below Fermi energy. On the other hand, the DOS of minority spin is partly filled and there is a d_{z^2} DOS peak slightly above Fermi energy (unoccupied). Based on the second order perturbation theory shown in equations (4)–(6), the possible nonzero

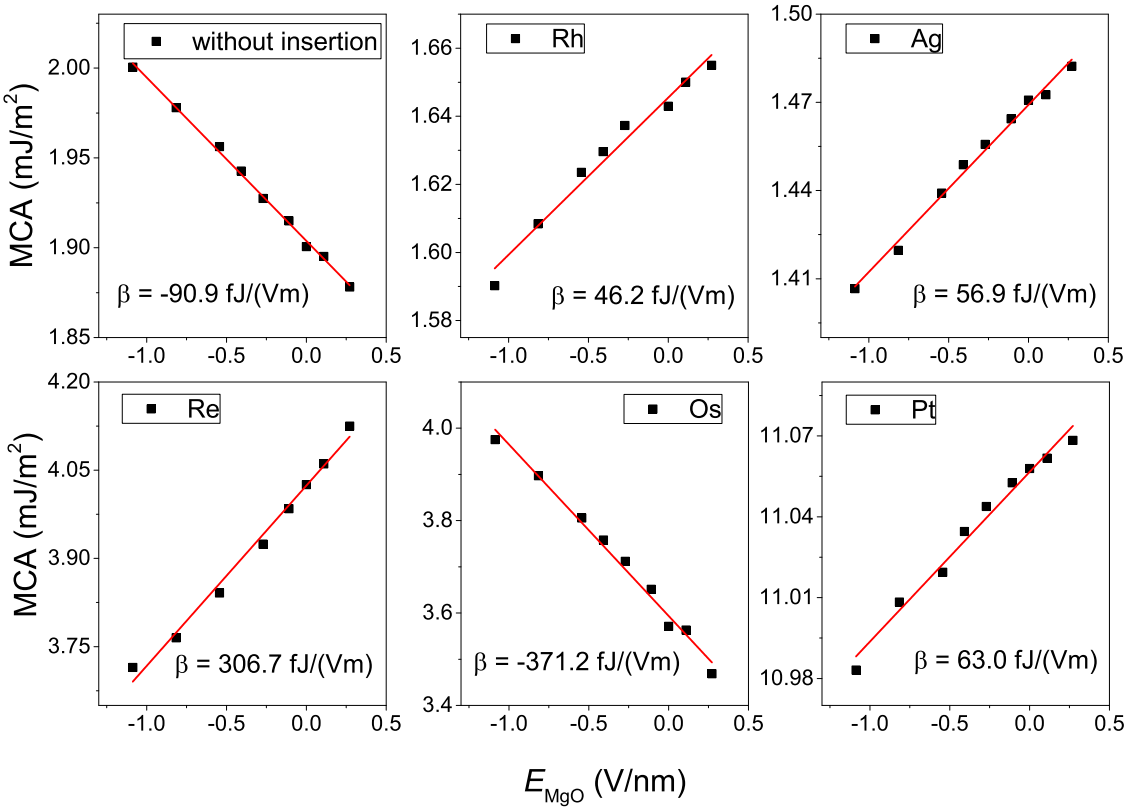

Figure 5. The MCA versus the applied electric field in MgO for Ta/Fe/X/MgO without and with insertions X = Pt, Rh, Ag, Re and Os. The slope of the MCA variation is evaluated in the linear response region.

energy correction could occur between occupied majority (d_{xy}, d_{yz}, d_{xz}) and unoccupied minority d_{z^2}. As we discussed in appendix A, for $\boldsymbol{M}$ along z direction (M_z), there are two non-vanishing $(\vec{\sigma}\cdot\vec{L})$ matrix elements involved the mentioned d-orbitals $\langle d_{yz}|\,(\vec{\sigma}\cdot\vec{L})^{\uparrow\downarrow}_{M_z}\,|d_{z^2}\rangle = -\mathrm{i}\sqrt{3}$ and $\langle d_{xz}|\,(\vec{\sigma}\cdot\vec{L})^{\uparrow\downarrow}_{M_z}\,|d_{z^2}\rangle = \sqrt{3}$, while for $\boldsymbol{M}$ along x direction (M_x) there is only one non-vanishing $(\vec{\sigma}\cdot\vec{L})$ matrix element $\langle d_{xz}|\,(\vec{\sigma}\cdot\vec{L})^{\uparrow\downarrow}_{M_x}\,|d_{z^2}\rangle = \sqrt{3}$. From this observation, one can conclude that there should be a large energy correction between majority d_{yz} and minority d_{z^2} orbitals for M_z while this energy correction is missing for M_x. In consequence, this would contribute to the positive MCA. This conjecture can be further examined by plotting the orbital resolved MCA contribution on Pt as shown in figure 3(c). Indeed, it is clearly seen that the major contribution to the PMA on Pt is from the pair of (d_{yz}, d_{z^2}).

In the following, we perform calculations on VCMA of Ta(7 ML)/Fe(3 ML)/X(1 ML)/MgO(3 ML)/vacuum with several insertion layers (X = Rh, Ag, Re, Os, Pt) which have relative large or similar PMA compared with Fe/MgO (figure 2(b)). In the present calculations, the electric field is introduced by using the dipole layer placed in the vacuum region of the supercell [30]. We first need to check whether the desired electric field has been applied correctly.

Figure 4 shows the change in the planar-averaged electrostatic potential across the Ta/Fe/Pt/MgO supercell when electric fields in vacuum $E_{\mathrm{vac}} = \pm 1$ V nm^{-1} are applied. It is clear that the potential drop occurring in the MgO and vacuum, whereas it is screened in the metallic Ta/Fe/Pt layers. The electric field inside of MgO is smaller than that in vacuum due to the large dielectric constant of MgO. The magnitude of electric field in MgO and vacuum has the relation: $E_{\mathrm{MgO}} = E_{\mathrm{vac}}/\varepsilon_{\mathrm{MgO}}$, where $\varepsilon_{\mathrm{MgO}}$ is the dielectric constant of MgO and E_{vac} is the electric field in vacuum. From figure 4, the dielectric constant of MgO can be estimated to be $\varepsilon_{\mathrm{MgO}} = E_{\mathrm{vac}}/E_{\mathrm{MgO}} = 3.68$. This value is smaller than the experimental value of $\varepsilon_{\mathrm{MgO}} = 9.5$. That is because only the electric part contribution to dielectric constant is included while the ionic contribution is not included in calculations.

We now consider the changes in the MCA of Ta/Fe/X/MgO (X = Rh, Ag, Re, Os, Pt) induced by an electric field in vacuum in the range of -4 to $+1$ V nm^{-1} (We notice that the electronic structures do not converge when E_{vac} is larger than $+2$ V nm^{-1}). In all our calculations, we do not relax the atomic structure in the presence of the electric field. The effect of the electric field on the MCA is quantified by the slope β in the linear range as MCA $= \beta E_{\mathrm{MgO}}$. Figure 5 shows the variation of the MCA energy as a function of electric field in MgO for structures with Rh, Ag, Re, Os and Pt interlayers. In the range of investigated electric field, the MCA is nearly a linear curve versus the electric field. Considering the dielectric constant of MgO as 3.68 (calculated from figure 4), the VCMA coefficient β can be extracted by linear fitting. First, we find that $|\beta|$ for

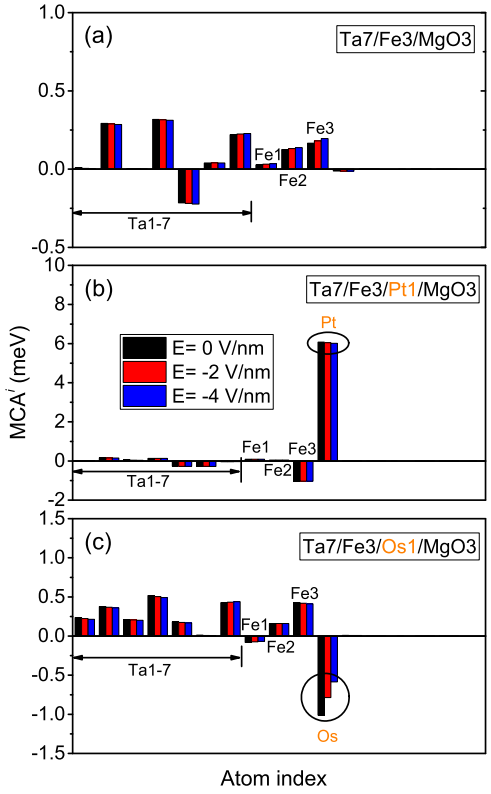

Figure 6. Layer-resolved contribution to MCA for (a) Ta/Fe/MgO, (b) Ta/Fe/Pt/MgO, and (c) Ta/Fe/Os/MgO under electric field $E_{\mathrm{vac}} = 0$ (black), -2 V nm^{-1} (red) and -4 V nm^{-1} (blue).

Pt, Rh and Ag are reduced in compared with that for the ideal Fe/MgO interface with $\beta = -90.9$ fJ V^{-1} m^{-1}. The reduction and sign reversal of VCMA with Pt interlayer agree with previous calculation results [18, 19]. More importantly, a large increase in the VCMA coefficients β for Re (306.7 fJ V^{-1} m^{-1}) and Os (-371.2 fJ V^{-1} m^{-1}) inserted layers are found, by a factor of 3.37 and 4.08, respectively. If we take the experimental dielectric constant of MgO $\varepsilon_{\mathrm{MgO}} = 9.5$, the VCMA coefficients β are 790 fJ V^{-1} m^{-1} and 960 fJ V^{-1} m^{-1} for structures with Re and Os interlayers, respectively. These results demonstrate that the enhancement of both the PMA and VCMA efficiency in the Ta/Fe/X/MgO stack is available by the Re and Os layers.

In order to gain more insight into the VCMA effect, the layer-resolved contribution to MCA under various electric fields for Ta/Fe/MgO, Ta/Fe/Pt/MgO and Ta/Fe/Os/MgO interfaces have been calculated and shown in figure 6. One can observe that, the response of MCA on external electric field mainly depends on the layers localized at the interfaces of Fe/MgO and Fe/X/MgO. That is, for Ta/Fe/MgO, the electric field induced change of MCA is mainly on the Fe layer, while with insertions, the VCMA effect is mainly transferred onto Pt and Os layers. Under increasing negative electric field, the MCA contribution of Fe layers in Ta/Fe/MgO interface increases and thus leading to a negative VCMA coefficient β. While for Pt interlayer, suppressed decreasing trend of MCA on Pt layer lead to a smaller and reversal VCMA coefficient β. For Ta/Fe/Os/MgO interface, the pronounced decrease of negative contribution to MCA of Os layer leads to an increase of MCA and results in an enhanced negative VCMA coefficient β. The reason for different VCMA coefficients for Pt and Os interlayers may be qualitatively understood by considering the different electronic properties of Pt and Os. As we know, the Pt has more itinerant *sp*-like electrons than Os at the Fermi energy. When the electric field is applied, the response of *sp* electrons does not contribute to the MCA and thus to VCMA effect. A qualitative conclusion may be that, the interlayer with more localized *d*-like electron may produce larger VCMA effect.

4. Summary

In summary, the MCA and VCMA of the Ta/Fe/X/MgO heterostructures have been investigated by first-principles calculations, where X is ML of 4*d* (Zr, Nb, Mo, Tc, Ru, Rh, Pd, Ag) and 5*d* (Hf, Ta, W, Re, Os, Ir, Pt, Au) transition metals. The MCA and VCMA dramatically depend on the X insertion, which has large SOC and becomes magnetic induced by the hybridization to the Fe layer. Among the investigated elements, two interfacial 5*d* metal layers Re and Os yield large enhancement of both PMA at zero field and VCMA coefficient. The response of MCA on external electric field mainly relies on the interfacial layers. Heavy metallic interlayer with large SOC constant and more *d*-like feature may benefit for the enhanced VCMA effect at Fe/MgO interface. At the same time, the thickness of insertion layer (around one ML) is much thinner than its spin diffusion length, so the degradation of tunneling magnetoresistance in MgO-based MTJs caused by inserted layer would be insignificant. These theoretical findings serve as simple guiding rules for future material structure design with enhanced PMA and VCMA, which may be important for high-speed and energy-efficient magnetoelectric device applications.

Acknowledgments

Long You is supported by the National Natural Science Foundation of China with Grant Nos. 61674062 and 61821003. Jia Zhang is supported by the National Natural Science Foundation of China with Grant No. 11704135. Computations were partly performed by utilizing TianHe-2 at the National Supercomputer Center in Guangzhou, China and the Platform for Data-Driven Computational Materials Discovery at the Songshan Lake Materials Laboratory, Dongguan, China.

Appendix A. The matrix element of H_{SOC} in the basis of *d* orbitals

The SOC Hamiltonian H_{soc} and $\vec{\sigma} \cdot \vec{L}$ operator are generally dependant on the magnetization orientation $M(\theta, \phi)$:

$$H_{\mathrm{soc}} = \xi(\vec{\sigma} \cdot \vec{L})_{M(\theta,\phi).} \tag{A1}$$

For instance, when the magnetization M is along z direction (Mz), the $\vec{\sigma}\cdot\vec{L}$ operator can be expressed in the matrix form of angular momentum operator:

$$(\vec{\sigma}\cdot\vec{L})_{M_z}=\begin{pmatrix} l_z & l_x-\mathrm{i}l_y \\ l_x+\mathrm{i}l_y & -l_z \end{pmatrix}. \tag{A2}$$

The SOC Hamiltonian and $\vec{\sigma}\cdot\vec{L}$ operator for a general magnetization direction $M(\theta,\phi)$ can be evaluated by a rotation matrix $u(\theta,\phi)$:

$$u(\theta,\phi)=\begin{pmatrix} \mathrm{e}^{-\mathrm{i}\phi/2}\cos(\theta/2) & -\mathrm{e}^{-\mathrm{i}\phi/2}\sin(\theta/2) \\ \mathrm{e}^{\mathrm{i}\phi/2}\sin(\theta/2) & \mathrm{e}^{\mathrm{i}\phi/2}\cos(\theta/2) \end{pmatrix}. \tag{A3}$$

It can be obtained by the following transformation:

$$\begin{aligned}(\vec{\sigma}\cdot\vec{L})_{M(\theta,\phi)} &= u(\theta,\phi)(\vec{\sigma}\cdot\vec{L})_{M_z}u^{\dagger}(\theta,\phi) \\ &= \begin{pmatrix} (\vec{\sigma}\cdot\vec{L})^{\uparrow\uparrow}_{M(\theta,\phi)} & (\vec{\sigma}\cdot\vec{L})^{\uparrow\downarrow}_{M(\theta,\phi)} \\ (\vec{\sigma}\cdot\vec{L})^{\downarrow\uparrow}_{M(\theta,\phi)} & (\vec{\sigma}\cdot\vec{L})^{\downarrow\downarrow}_{M(\theta,\phi)} \end{pmatrix}. \end{aligned} \tag{A4}$$

For instance, when the magnetization $\boldsymbol{M}$ is along x axis (M_x), the corresponding Euler angles are $\theta=\pi/2$, $\phi=0$, then the expression of $\vec{\sigma}\cdot\vec{L}$ for M_x should be:

$$(\vec{\sigma}\cdot\vec{L})_{M_x}=\begin{pmatrix} -l_x & l_z-\mathrm{i}l_y \\ l_z+\mathrm{i}l_y & l_x \end{pmatrix}. \tag{A5}$$

The matrix element of orbital angular momentum l_x, l_y and l_z in the basis of d_{xy}, d_{yz}, d_{xz}, d_{z^2}, $d_{x^2-y^2}$ can be evaluated by constructing those d orbitals with the linear combinations of complex spherical harmonics Y_{lm}:

$$\begin{aligned} &d_{xy}=-\frac{\mathrm{i}}{\sqrt{2}}(Y_{22}-Y_{2-2}); \quad d_{yz}=\frac{1}{\sqrt{2}}(Y_{21}+Y_{2-1}); \\ &d_{xz}=\frac{1}{\sqrt{2}}(Y_{21}-Y_{2-1}); \quad d_{x^2-y^2}=\frac{1}{\sqrt{2}}(Y_{22}+Y_{2-2}); \\ &d_{z^2}=Y_{20}. \end{aligned} \tag{A6}$$

The matrix elements of angular momentum l_x, l_y and l_z in the d orbital order of (d_{xy}, d_{yz}, d_{xz}, d_{z^2},$d_{x^2-y^2}$) can be easily computed as follows:

$$l_x=\begin{pmatrix} & |d_{xy}\rangle & |d_{yz}\rangle & |d_{xz}\rangle & |d_{z^2}\rangle & |d_{x^2-y^2}\rangle \\ \langle d_{xy}| & 0 & 0 & -\mathrm{i} & 0 & 0 \\ \langle d_{yz}| & 0 & 0 & 0 & -\mathrm{i}\sqrt{3} & -\mathrm{i} \\ \langle d_{xz}| & \mathrm{i} & 0 & 0 & 0 & 0 \\ \langle d_{z^2}| & 0 & \mathrm{i}\sqrt{3} & 0 & 0 & 0 \\ \langle d_{x^2-y^2}| & 0 & \mathrm{i} & 0 & 0 & 0 \end{pmatrix} l_y=\begin{pmatrix} & |d_{xy}\rangle & |d_{yz}\rangle & |d_{xz}\rangle & |d_{z^2}\rangle & |d_{x^2-y^2}\rangle \\ \langle d_{xy}| & 0 & \mathrm{i} & 0 & 0 & 0 \\ \langle d_{yz}| & -\mathrm{i} & 0 & 0 & 0 & 0 \\ \langle d_{xz}| & 0 & 0 & 0 & \mathrm{i}\sqrt{3} & -\mathrm{i} \\ \langle d_{z^2}| & 0 & 0 & -\mathrm{i}\sqrt{3} & 0 & 0 \\ \langle d_{x^2-y^2}| & 0 & 0 & \mathrm{i} & 0 & 0 \end{pmatrix}$$

$$l_z=\begin{pmatrix} & |d_{xy}\rangle & |d_{yz}\rangle & |d_{xz}\rangle & |d_{z^2}\rangle & |d_{x^2-y^2}\rangle \\ \langle d_{xy}| & 0 & 0 & 0 & 0 & 2\mathrm{i} \\ \langle d_{yz}| & 0 & 0 & \mathrm{i} & 0 & 0 \\ \langle d_{xz}| & 0 & -\mathrm{i} & 0 & 0 & 0 \\ \langle d_{z^2}| & 0 & 0 & 0 & 0 & 0 \\ \langle d_{x^2-y^2}| & -2\mathrm{i} & 0 & 0 & 0 & 0 \end{pmatrix}. \tag{A7}$$

Then we have the matrix elements of $\vec{\sigma}\cdot\vec{L}$ operator for $\boldsymbol{M}$ along z direction (M_z):

$$(\vec{\sigma}\cdot\vec{L})^{\uparrow\uparrow}_{M_z}=l_z; \quad (\vec{\sigma}\cdot\vec{L})^{\uparrow\downarrow}_{M_z}=l_x-\mathrm{i}l_y=\begin{pmatrix} & |d_{xy}\rangle & |d_{yz}\rangle & |d_{xz}\rangle & |d_{z^2}\rangle & |d_{x^2-y^2}\rangle \\ \langle d_{xy}| & 0 & 1 & -\mathrm{i} & 0 & 0 \\ \langle d_{yz}| & -1 & 0 & 0 & -\mathrm{i}\sqrt{3} & -\mathrm{i} \\ \langle d_{xz}| & \mathrm{i} & 0 & 0 & \sqrt{3} & -1 \\ \langle d_{z^2}| & 0 & \mathrm{i}\sqrt{3} & -\sqrt{3} & 0 & 0 \\ \langle d_{x^2-y^2}| & 0 & \mathrm{i} & 1 & 0 & 0 \end{pmatrix}. \tag{A8}$$

And similarly we can obtain the matrix elements of $\vec{\sigma}\cdot\vec{L}$ operator for $\boldsymbol{M}$ along x direction (M_x):

$$(\vec{\sigma}\cdot\vec{L})^{\uparrow\uparrow}_{M_x}=-l_x; \quad (\vec{\sigma}\cdot\vec{L})^{\uparrow\downarrow}_{M_x}=l_z-\mathrm{i}l_y=\begin{pmatrix} & |d_{xy}\rangle & |d_{yz}\rangle & |d_{xz}\rangle & |d_{z^2}\rangle & |d_{x^2-y^2}\rangle \\ \langle d_{xy}| & 0 & 1 & 0 & 0 & 2\mathrm{i} \\ \langle d_{yz}| & -1 & 0 & \mathrm{i} & 0 & 0 \\ \langle d_{xz}| & 0 & -\mathrm{i} & 0 & \sqrt{3} & -1 \\ \langle d_{z^2}| & 0 & 0 & -\sqrt{3} & 0 & 0 \\ \langle d_{x^2-y^2}| & -2\mathrm{i} & 0 & 1 & 0 & 0 \end{pmatrix}. \tag{A9}$$

When magnetization is along other general direction $M(\theta, \phi)$, the matrix elements of $\vec{\sigma}\cdot\vec{L}$ operator can be obtained by rotation transformations in equation (A4)

$$(\vec{\sigma}\cdot\vec{L})^{\uparrow\uparrow}_{M(\theta,\phi)} = \begin{pmatrix} & |d_{xy}\rangle & |d_{yz}\rangle & |d_{xz}\rangle & |d_{z^2}\rangle & |d_{x^2-y^2}\rangle \\ \langle d_{xy}| & 0 & \mathrm{i}\,\sin\,\theta\,\sin\,\phi & -\mathrm{i}\,\sin\,\theta\,\cos\,\phi & 0 & 2\mathrm{i}\,\cos\,\theta \\ \langle d_{yz}| & -\mathrm{i}\,\sin\,\theta\,\sin\,\phi & 0 & \mathrm{i}\,\cos\,\theta & -\mathrm{i}\sqrt{3}\,\sin\,\theta\,\cos\,\phi & -\mathrm{i}\,\sin\,\theta\,\cos\,\phi \\ \langle d_{xz}| & \mathrm{i}\,\sin\,\theta\,\cos\,\phi & -\mathrm{i}\,\cos\,\theta & 0 & \mathrm{i}\sqrt{3}\,\sin\,\theta\,\sin\,\phi & -\mathrm{i}\,\sin\,\theta\,\sin\,\phi \\ \langle d_{z^2}| & 0 & \mathrm{i}\sqrt{3}\,\sin\,\theta\,\cos\,\phi & -\mathrm{i}\sqrt{3}\,\sin\,\theta\,\sin\,\phi & 0 & 0 \\ \langle d_{x^2-y^2}| & -2\mathrm{i}\,\cos\,\theta & \mathrm{i}\,\sin\,\theta\,\cos\,\phi & \mathrm{i}\,\sin\,\theta\,\sin\,\phi & 0 & 0 \end{pmatrix},$$

$$(\vec{\sigma}\cdot\vec{L})^{\downarrow\downarrow}_{M(\theta,\phi)} = \begin{pmatrix} & |d_{xy}\rangle & |d_{yz}\rangle & |d_{xz}\rangle & |d_{z^2}\rangle & |d_{x^2-y^2}\rangle \\ \langle d_{xy}| & 0 & \mathrm{i}\,\cos\,\theta\,\sin\,\phi+\cos\,\phi & -\mathrm{i}\,\cos\,\theta\,\cos\,\phi+\sin\,\phi & 0 & -2\mathrm{i}\,\sin\,\theta \\ \langle d_{yz}| & -\mathrm{i}\,\cos\,\theta\,\sin\,\phi-\cos\,\phi & 0 & -\mathrm{i}\,\sin\,\theta & \sqrt{3}(-\mathrm{i}\,\cos\,\theta\,\cos\,\phi+\sin\,\phi) & -\mathrm{i}\,\cos\,\theta\,\cos\,\phi+\sin\,\phi \\ \langle d_{xz}| & \mathrm{i}\,\cos\,\theta\,\cos\,\phi-\sin\,\phi & \mathrm{i}\,\sin\,\theta & 0 & \sqrt{3}(\cos\,\phi+\mathrm{i}\,\cos\,\theta\,\sin\,\phi) & -\mathrm{i}\,\cos\,\theta\,\sin\,\phi-\cos\,\phi \\ \langle d_{z^2}| & 0 & \sqrt{3}(\mathrm{i}\,\cos\,\theta\,\cos\,\phi-\sin\,\phi) & -\sqrt{3}(\cos\,\phi+\mathrm{i}\,\cos\,\theta\,\sin\,\phi) & 0 & 0 \\ \langle d_{x^2-y^2}| & 2\mathrm{i}\,\sin\,\theta & \mathrm{i}\,\cos\,\theta\,\cos\,\phi-\sin\,\phi & \mathrm{i}\,\cos\,\theta\,\sin\,\phi+\cos\,\phi & 0 & 0 \end{pmatrix}. \tag{A10}$$

The other two matrix elements of $\vec{\sigma}\cdot\vec{L}$ operator can be obtained by the following relations:

$$(\vec{\sigma}\cdot\vec{L})^{\downarrow\downarrow}_{M(\theta,\phi)} = -(\vec{\sigma}\cdot\vec{L})^{\uparrow\uparrow}_{M(\theta,\phi)}; \quad (\vec{\sigma}\cdot\vec{L})^{\downarrow\uparrow}_{M(\theta,\phi)} = \left[(\vec{\sigma}\cdot\vec{L})^{\uparrow\downarrow}_{M(\theta,\phi)}\right]^{\dagger}. \tag{A11}$$

Appendix B. The SOC and layer resolved SOC energy in VASP–PAW theory framework

By taking the SOC into account, the full Hamiltonian H of electrons can be written as:

$$H = H_0 + H_{\mathrm{soc}}, \tag{B1}$$

where H_0 is the Hamiltonian without SOC and H_{soc} is the SOC Hamiltonian as it is shown in equation (A1).

The solution of above full Hamiltonian H is a 2×1 spinor:

$$|\psi_n\rangle = \begin{pmatrix} |\psi_n^1\rangle \\ |\psi_n^2\rangle \end{pmatrix}, \tag{B2}$$

where n is energy band index.

On the other hand, the all-electron (AE) wavefunction in the PAW theory frame can be expressed in terms of pseudo-electron (PE) wave function [39]:

$$\left|\psi_n^{\alpha}\right\rangle = \left|\tilde{\psi}_n^{\alpha}\right\rangle + \sum_i (|\phi_i\rangle - \left|\tilde{\phi}_i\right\rangle)\left\langle \tilde{p}_i \middle| \tilde{\psi}_n^{\alpha}\right\rangle, \tag{B3}$$

where $|\phi_i\rangle(|\tilde{\phi}_i\rangle)$ is the AE (PE) atomic wavefunction and $|\psi_n^{\alpha}\rangle(|\tilde{\psi}_n^{\alpha}\rangle)$is the AE (PE) Bloch wavefunction ($\alpha = 1, 2$), $|\tilde{p}_i\rangle$is the projector, i is a shorthand index for atomic sites a, reference pseudo energy ε, and orbital and magnetic quantum number (l, m), that is $i = (a_i, \varepsilon_i, l, m)$.

According to PAW theory, the AE wave function inside of the augmentation sphere can be expanded by AE atomic wave function as follows:

$$|\psi_n^{\alpha}\rangle = \sum_i |\phi_i\rangle \left\langle \tilde{p}_i \middle| \tilde{\psi}_n^{\alpha}\right\rangle, \tag{B4}$$

and outside of the augmentation sphere, the AE and PE wave functions will be the same:

$$|\psi_n^{\alpha}\rangle = |\tilde{\psi}_n^{\alpha}\rangle. \tag{B5}$$

The SOC energy can be evaluated as follow:

$$E_{\mathrm{soc}} = \sum_n \langle\psi_n|H_{\mathrm{soc}}|\psi_n\rangle = \sum_n \sum_{\alpha,\beta=1,2} \langle\psi_n^{\alpha}|H_{\mathrm{soc}}^{\alpha\beta}|\psi_n^{\beta}\rangle. \tag{B6}$$

By considering that the radius dependant SOC strength $\xi(r) = \frac{\hbar^2}{4m^2c^2r}\frac{\mathrm{d}V(r)}{\mathrm{d}r}$ (and therefore H_{soc}) is well-localized around the atomic nuclei center, the SOC energy expressed in equation (B6) can be evaluated only inside of augmentation sphere by inserting equation (B4) into (B6). Therefore, the SOC energy can be calculated as:

$$\begin{aligned} E_{\mathrm{soc}} &= \sum_{i,j}^{\alpha,\beta} \sum_n \left\langle \tilde{\psi}_n^{\alpha} \middle| \tilde{p}_i \right\rangle \left\langle \tilde{p}_j \middle| \tilde{\psi}_n^{\beta} \right\rangle \langle\phi_i| H_{\mathrm{soc}}^{\alpha,\beta} |\phi_j\rangle \\ &= \sum_{i,j}^{\alpha,\beta} \rho_{i,j}^{\alpha,\beta} D_{i,j}^{\alpha,\beta}, \end{aligned} \tag{B7}$$

where $\rho_{i,j}^{\alpha,\beta}$ is the occupancy of each augmentation channel (i, j) [39]:

$$\rho_{i,j}^{\alpha,\beta} = \sum_n \langle\tilde{\psi}_n^{\alpha}|\tilde{p}_i\rangle \left\langle \tilde{p}_j \middle| \tilde{\psi}_n^{\beta}\right\rangle, \tag{B8}$$

and $D_{i,j}$ is SOC contribution to the so-called D matrix (2×2) which enters into the noncollinear Kohn–Sham Hamiltonian [39]:

$$D_{i,j} = \langle\phi_i| H_{\mathrm{soc}} |\phi_j\rangle. \tag{B9}$$

Again, by considering the fact that H_{soc} is well-localized around the atomic center, the nonvanishing D matrix in equation (B9) should be on-site and share the same orbital angular momentum l. By inserting $|\phi_i\rangle = R_{l,\varepsilon_i}(r)|l,m\rangle$ into equation (B9), we obtain:

$$D_{i,j} = \delta_{a_i,a_j}\delta_{l_i=l,l_j}\xi_{\varepsilon_i,\varepsilon_j}^{a_i,l} \langle l,m|\,\vec{\sigma}\cdot\vec{L}\,|l,m'\rangle, \tag{B10}$$

$\xi_{\varepsilon_i,\varepsilon_j}^{a_i,l} = \int R_{l,\varepsilon_i}(r)R_{l,\varepsilon_j}(r)\xi^{a_i}(r)r^2\mathrm{d}r$ is the pseudo energy dependent SOC constant, and the matrix element $\langle l,m|\,\vec{\sigma}\cdot\vec{L}\,|l,m'\rangle$ has been discussed in appendix A.

Finally, the SOC energy expressed in equation (B7) can be calculated by summarizing the contribution on individual atom as:

$$E_{\mathrm{soc}} = \sum_{a} E^{a}_{\mathrm{soc}} = \sum_{a}\Big(\sum_{l}\sum_{m,m'} E^{a,l,m,m'}_{\mathrm{soc}}\Big), \tag{B11}$$

where E^{a}_{soc} is the atom (a is the atom index) resolved SOC energy, $E^{a,l,m,m'}_{\mathrm{soc}}$ is the atom, orbital, magnetic quantum number resolved SOC energy.

$$E^{a,l,m,m'}_{\mathrm{soc}} = \sum_{\alpha,\beta} \rho^{\alpha,\beta}_{i,j}\, \xi^{a_i,l}_{\varepsilon_i,\varepsilon_j} \langle l,m|\, \vec{\sigma}\cdot\vec{L}|l,m'\rangle^{\alpha\beta}. \tag{B12}$$

ORCID iDs

Jia Zhang https://orcid.org/0000-0002-4125-2269

References

[1] Matsukura F, Tokura Y and Ohno H 2015 *Nat. Nanotechnol.* **10** 209
[2] Tsymbal E Y 2012 *Nat. Mater.* **11** 12
[3] Miwa S, Suzuki M, Tsujikawa M, Nozaki T, Nakamura T, Shirai M, Yuasa S and Suzuki Y 2019 *J. Phys. D: Appl. Phys.* **52** 063001
[4] Nozaki T, Yamamoto T, Miwa S, Tsujikawa M, Shirai M, Yuasa S and Suzuki Y 2019 *Micromachines* **10** 327
[5] Kang W, Ran Y, Zhang Y, Lv W and Zhao W 2017 *IEEE Trans. Nanotechnol.* **16** 387–95
[6] Butler W H, Zhang X G, Schulthess T C and Maclaren J M 2001 *Phys. Rev.* B **63** 054416
[7] Yuasa S, Nagahama T, Fukushima A, Suzuki Y and Ando K 2004 *Nat. Mater.* **3** 868–71
[8] Yang H X, Chshiev M, Dieny B, Lee J H, Manchon A and Shin K H 2011 *Phys. Rev.* B **84** 054401
[9] Niranjan M K, Duan C G, Jaswal S S and Tsymbal E Y 2010 *Appl. Phys. Lett.* **96** 222504
[10] Maruyama T *et al* 2009 *Nat. Nanotechnol.* **4** 158–61
[11] Miwa S, Matsuda K, Tanaka K, Kotani Y, Goto M, Nakamura T and Suzuki Y 2015 *Appl. Phys. Lett.* **107** 162402
[12] Zhang J, Franz C, Czerner M and Heiliger C 2014 *Phys. Rev.* B **90** 184409
[13] Zhang J, Lukashev P V, Jaswal S S and Tsymbal E Y 2017 *Phys. Rev.* B **96** 014435
[14] Bauer U, Yao L, Tan A J, Agrawal P, Emori S, Tuller H L, Dijken S v and Beach G S D 2015 *Nat. Mater.* **14** 174
[15] Rajanikanth A, Hauet T, Montaigne F, Mangin S and Andrieu S 2013 *Appl. Phys. Lett.* **103** 062402
[16] Bauer U, Przybylski M, Kirschner J and Beach G S 2012 *Nano Lett.* **12** 1437
[17] Nozaki T *et al* 2016 *Phys. Rev. Appl.* **5** 044006
[18] Tsujikawa M, Haraguchi S and Oda T 2012 *J. Appl. Phys.* **111** 083910
[19] Nakamura K, Nomura T, Pradipto A M, Nawa K, Akiyama T and Ito T 2017 *J. Magn. Magn. Mater.* **429** 214
[20] Odkhuu D, Rhim S H, Park N and Hong S C 2013 *Phys. Rev.* B **88** 184405
[21] Bonaedy T, Choi J W, Jang C, Min B C and Chang J 2015 *J. Phys. D: Appl. Phys.* **48** 225002
[22] Miwa S *et al* 2017 *Nat. Commun.* **8** 15848
[23] Iida Y *et al* 2020 *J. Phys. D: Appl. Phys.* **53** 124001
[24] Nozaki T, Yamamoto T, Tamaru S, Kubota H, Fukushima A, Suzuki Y and Yuasa S 2018 *APL Mater.* **6** 026101
[25] Nozaki T *et al* 2017 *NPG Asia Mater.* **9** e451
[26] Nozaki T *et al* 2020 *APL Mater.* **8** 011108
[27] Hibino Y *et al* 2016 *Appl. Phys. Lett.* **109** 082403
[28] Shukla A K, Goto M, Xu X, Nawaoka K, Suwardy J, Ohkubo T, Hono K, Miwa S and Suzuki Y 2018 *Sci. Rep.* **8** 10362
[29] Suwardy J, Nawaoka K, Cho J, Goto M, Suzuki Y and Miwa S 2018 *Phys. Rev.* B **98** 144432
[30] Neugebauer J and Scheffler M 1992 *Phys. Rev.* B **46** 16067
[31] Blöchl P E 1994 *Phys. Rev.* B **50** 17953
[32] Kresse G and Joubert D 1999 *Phys. Rev.* B **59** 1758
[33] Perdew J P, Burke K and Ernzerhof M 1996 *Phys. Rev. Lett.* **77** 3865
[34] He K H, Chen J S and Feng Y P 2011 *Appl. Phys. Lett.* **99** 072503
[35] He K H and Chen J S 2012 *J. Appl. Phys.* **111** 07C109
[36] Antropov V, Ke L and Aberg D 2014 *Solid State Commun.* **194** 35
[37] Wang D S, Wu R and Freeman A J 1993 *Phys. Rev.* B **47** 22
[38] Laan G V d 1998 *J. Phys.: Condens. Matter* **10** 3239
[39] Hobbs D, Kresse G and Hafner J 2000 *Phys. Rev.* B **62** 11556